Journal of Materials Chemistry A

Electrolyte Strategies to Minimize Surface Reactivity for Improved Reversibility of H2 – H3 Phase Transition

Journal:	*Journal of Materials Chemistry A*
Manuscript ID	TA-ART-07-2024-005216.R2
Article Type:	Paper
Date Submitted by the Author:	25-Sep-2024
Complete List of Authors:	Adamo, J. Brandon; The University of Texas at Austin Manthiram, Arumugam; The University of Texas at Austin, Materials Science and Engineering

ARTICLE

Electrolyte Strategies to Minimize Surface Reactivity for Improved Reversibility of the H2 – H3 Phase Transition

Received 00th January 20xx,
Accepted 00th January 20xx

DOI: 10.1039/x0xx00000x

J.Brandon Adamo[a] and Arumugam Manthiram[a]

High-nickel layered oxide cathodes are promising candidates for application in next-generation lithium-ion batteries. However, they are plagued by high surface reactivity with electrolytes and poor reversibility of the high voltage H2 – H3 phase transition. While electrolytes generally impact cathode surface reactivity, herein we demonstrate that the use of advanced electrolytes can greatly improve the reversibility of the bulk H2 – H3 phase transition due to a reduction in surface reactivity and resultant surface reconstruction. We compare the ability of several common electrolyte enhancement strategies to improve the reversibility of the H2 – H3 phase transition with a $LiNiO_2$ cathode. We find that while all strategies tested in this study improve the reversibility of the phase transition, a combination of fluorinated solvents and an $LiPO_2F_2$ additive yields the best results in galvanostatic cycling. We quantitatively measure the capacity loss in the H2 – H3 phase transition region with second derivative analysis and show that the degree of capacity fade is different in different phase transition regions. With galvanostatic intermittent titration technique and galvanostatic electrochemical impedance spectroscopy, we find that advanced electrolytes can reduce the resistance growth with cycling when passing through the H2 – H3 phase transition. With cyclic step chronoamperometry, we examine the evolution of the high-rate performance of the phase transition in each electrolyte and find that a combination of surface stabilization and conductivity are needed to optimize high-rate performance.

Introduction

Lithium-ion batteries are a potential cornerstone technology in the nascent shift to renewable energy.[1,2] Since their inception in the latter half of the 20th century, there has been a constant push to improve both their cyclability and energy density.[1,3,4] In pursuit of higher energy density, high-nickel layered oxide cathodes have garnered increasing interest from both academia and industry.[1,5,6] However, such cathodes seem to require a tradeoff between cycle life and single-cycle energy density.[6–8] This is due to various degradation mechanisms that acutely manifest at high states of charge (SOC), including surface reactivity, transition-metal-ion dissolution, and bulk phase transitions.[9–14]

Multiple strategies have been employed to mitigate the inherent issues of high-nickel layered oxide cathodes, including bulk doping, surface coating, and advanced electrolytes.[6,9,15] Of particular interest to this work are the various electrolyte strategies that have been shown to improve the cyclability of layered oxide cathodes. One such strategy is to increase the salt content in the electrolyte, resulting in a reduction in free solvent which can participate in side-reactions. Such electrolytes are known as high concentration electrolytes (HCE).[16–18] The increased salt content results in increased oxidative stability and cyclability, at the expense of viscosity and increased materials cost.[17,19] To mitigate this, researchers often add a non-solvating diluent to HCEs, which maintains the high concentration solvation structure, while lowering viscosity.[18–20] Such electrolytes are commonly known as localized high concentration electrolytes (LHCE). Another common and effective strategy is replacing standard solvents with fluorinated solvents, which have been shown to both lower solvation energy and help form an inorganic-rich cathode electrolyte interphase (CEI).[21–23] Such CEIs have been shown to better protect the particle surface from degradation.[23–25] Electrolytes that employ fluorinated solvents are referred to as highly fluorinated electrolytes (HFE). LHCEs have also been shown to yield inorganic-rich CEI layers.[14] In addition to modifying the salt content and solvents, various trace additives have been shown to improve performance by forming beneficial decomposition products on the electrode surface.[26–28] While each of these strategies has shown improved performance, their relative effectiveness in improving the reversibility of particular phase transitions in layered oxides has not as of yet been explored.

In high nickel layered oxide cathodes, the initial series of phase transitions are typified by a gradual expansion of the c-axis lattice parameter (CALP) and the associated interlayer spacing. [5,29,30] Resultantly, the phase transitions, Hexagonal 1(H1) – Monoclinic (M) seen at ~ 2.8 – 3.9 V and M – Hexagonal 2(H2) seen at ~ 3.9 V – 4.1 V, enjoy relatively facile lithium-ion

Materials Science and Engineering Program & Walker Department of Mechanical Engineering, University of Texas at Austin, Austin, Texas 78712, USA

[a] † E-mail: manth@austin.utexas.edu

[b] Electronic Supplementary Information (ESI) available: [details of any supplementary

[c] information available should be included here]. See DOI: 10.1039/x0xx00000x

diffusion as well as good reversibility.[7,8] The higher voltage H2 – Hexagonal 3 (H3) phase transition, however, inverts these trends, with a sharp contraction of the CALP leading to reduced lithium-ion diffusivity.[5,10,30] Along with the CALP contraction, the H2 – H3 phase transition region is notable for occurring at delithiation states, where the $Ni^{3+/4+}$ and $Co^{3+/4+}$ energy bands overlap with the O^{2-}:2p energy band.[2,31] This results in oxidation of oxide ions and consequentially irreversible release of oxygen from the layered oxide lattice.[2] The CALP contraction and increased reactivity results in reduced cyclability when charging and discharging through the H2 – H3 phase transition.[7,8,32] For these reasons, industry and researchers alike have, at times, opted to avoid this phase transition entirely to improve the overall cell cyclability.[7,8,32] This strategy, while effective, leaves ~ 1/5 of the potential capacity untapped, compared with a cell cycled to 4.4 V vs. Li/Li^+. As such, there is an inherent compromise that must be balanced between cyclability and energy density.

However, this compromise can be made easier by modifying various cell components to somewhat mitigate the inherent instability of the H2 – H3 phase transition. Coatings and bulk doping have been shown to "suppress" the phase transition.[33–35] However, such modifications require changes to cathode manufacturing processes. Electrolytes on the other hand are a relatively simple component to modify without impacting the overall cell assembly and cathode synthesis processes. Because electrolytes only interact directly with the surface of the electrodes, it may not seem obvious that they would affect bulk phenomena, such as phase transitions. However, electrolytes can impact the degree of surface reactivity and, therefore, surface reconstruction on the cathode. Since phase transitions in layered oxides initiate at the particle surface before nucleating into the bulk, the ease with which a phase transition may initiate and propagate can be greatly affected by the state of the electrode surface, which is strongly influenced by the electrolyte employed. [36] Despite this, it remains unclear the degree to which common electrolyte strategies improve the reversibility of the H2 – H3 phase transition.

In this work, we compare the reversibility of the H2 – H3 phase transition by pairing $LiNiO_2$ (LNO) cathodes with five electrolytes. One electrolyte is of a standard baseline composition, while the others employ the various strategies discussed above. After initially characterizing both the cathode material and electrolytes, we find through galvanostatic cycling and subsequent analyses that each of the four advanced electrolytes employed qualitatively improve the reversibility of the H2 – H3 phase transition. We proceed to show this quantitatively, with a second derivative analysis (SDA). Furthermore, the resistance growth experienced by LNO in each electrolyte after cycling is assessed with galvanostatic intermittent titration technique (GITT). The impedance is further examined dynamically with galvanostatic electrochemical impedance spectroscopy (GEIS). Lastly, the rate capability of LNO in each electrolyte through the H2 – H3 phase transition over cycling is examined with cyclic step chronoamperometry (CSCA). We find that while all the electrolytes tested effectively improve the reversibility of the phase transition, fluorinated solvents best preserve both the capacity and the kinetics of the H2 – H3 phase transition.

Experimental

Electrolyte Preparation

Electrolytes were prepared inside an Ar filled glovebox with H_2O and O_2 levels less than 0.1 ppm. LP57 was purchased from Gotion, and it is a 1 M solution of $LiPF_6$ in a 3:7 mixture of ethylene carbonate (EC) and ethyl methyl carbonate (EMC) by weight. Additional chemicals used to mix electrolytes include EC from Gotion, EMC from Gotion, Vinylene carbonate (VC) from Gotion, Monofluoroethylene carbonate (FEC) from Gotion, 1,1,2,2-Tetrafluoroethyl-2,2,2,3-tetrafluoropropyl ether (TTE) from Synquest, $LiPF_6$ salt from Gotion, Ferrocene (Fc) from Thermo Fischer, and $LiPO_2F_2$ (PFO) from Capchem. Once mixed, the electrolytes were given adequate time to fully homogenize before being used for experiments.

$LiNiO_2$ Preparation

LNO was prepared with the same method used in our previous work.[10,30,37] Nickel sulphate, from Alfa Aeser, was dissolved in deionized water and slowly added dropwise to a continuously stirred tank reactor (CSTR). A concentrated potassium hydroxide solution was simultaneously added to the CSTR to maintain the desired pH of ~ 11.6. A certain amount of ammonium hydroxide was also added dropwise to serve as a chelating agent. During the reaction, $Ni(OH)_2$ was formed and precipitated out of solution. After precipitating, the $Ni(OH)_2$ was washed with deionized water and dried. The $Ni(OH)_2$ precursor obtained was then mixed by hand in a mortar and pestle with a stoichiometric amount of LiOH plus 3 % excess and then calcined in a tube furnace with flowing oxygen. The furnace was first held at 500 ˚C for 5 h and then at 655 ˚C for an additional 12 h. After cooling to room temperature, the calcined LNO was reground to break up any agglomerates and then cast into electrodes.

Electrode and Cell Preparation

Electrodes were prepared by first mixing the prepared LNO powder with C65 conductive carbon from Alfa Aeser and poly(vinylidene fluoride) (PVDF) binder from Kynar in a 90 : 5 : 5 ratio. An appropriate amount of N-methyl-2-pyrrolidone (NMP) from Sigma Aldrich was added to achieve the needed viscosity. The slurry was then cast onto a carbon-coated aluminium foil and dried in a 110 ˚C drying oven for at least 15 minutes to evaporate the NMP. After the initial drying, the cast electrodes were calendared and dried overnight in a 110 ˚C vacuum oven. The LNO electrodes were cast to a nominal loading of 1 mA h cm^{-2}. $Li_4Ti_5O_{12}$ (LTO) from MSE Supplies was cast following the same procedure as with LNO. LTO electrodes were cast to a nominal loading of 1.2 mA h cm^{-2}.

Li-metal || LNO cells were made with the electrolyte of interest added to a 2032-coin cell containing a lithium-metal chip as the negative electrode, a single layer of Celgard 2325 as

a separator, and LNO as the positive electrode. Nickel foam was placed on top of the lithium metal to provide stack pressure. LTO || LNO cells were made with the electrolyte of interest with an LTO negative electrode, a single layer of Celgard 2325 as a separator, and LNO as the positive electrode. A stainless-steel conical spring and two 1-mm stainless steel spacers were used to provide stack pressure.

Characterization

Electrochemical cycling tests, including galvanostatic cycling, CSCA, and GITT were carried out on Arbin and Landt cyclers. A 1C rate was defined as 180 mA g^{-1} of active cathode material. GEIS, linear sweep voltammetry (LSV), and cyclic voltammetry (CV) tests were conducted on a Biologic VMP3 potentiostat. Fourier transform infrared spectroscopy (FTIR) analysis was carried out with a Thermo Scientific Nicolet iS5. X-ray diffraction (XRD) patterns were collected with a Rigaku Miniflex benchtop XRD. Scanning electron microscopy (SEM) and energy dispersive X-ray spectroscopy (EDX) images were gathered with a Vega Vescan3 instrument. Ionic conductivities were measured with a Mettler Toledo conductivity probe. Equivalent-circuit analysis was performed with EC-Lab software. Rietveld refinement was performed with GSAS-II software.

Galvanostatic Electrochemical Impedance Spectroscopy

GEIS tests were conducted by first charging the LTO || LNO cell of interest to 2.55 V vs. LTO (~ 4.1 V vs. Li/Li^+) and then holding the cell at 2.55 V until the cutoff current of C/50 was reached. The cells were then placed on a Biologic VMP3 potentiostat and charged at a C/20 rate to a cutoff voltage of 3.2 V vs. LTO (~ 4.75 V vs. Li/Li^+). After reaching the upper cutoff voltage, the cells were discharged at a C/20 rate. GEIS patterns were collected continuously, during cycle with a 10-mV perturbation from 500 kHz to 10 mHz.

Linear Sweep Voltammetry

LSV tests were conducted by building Li || carbon-coated current collector cells with the electrolyte of interest. The cells were then swept at 3.25 – 5 V at 0.05 mV s^{-1} and the current response was recorded.

Solvation Energy Measurements

Solvation energy tests were conducted, similar to other studies, by adding a small amount of Fc to the electrolyte to bring the Fc concentration to 10 mM.[38,39] The Fc-containing electrolytes were then placed in cells with a lithium-metal anode, separator, and nickel foil as a counter electrode. CV tests were then conducted and the apparent ferrocene/ ferrocenium (Fc/Fc^+) potential was measured.

Results and Discussion

After synthesis, we gathered the XRD pattern of LNO as shown in Figure 1a. The synthesized LNO displays the typical α-$NaFeO_2$ structure with the $R\bar{3}m$ space group. [6,30] No impurity phases were detected in the XRD pattern. The Rietveld refinement results are presented in Figure S1. We selected LNO as it has the highest possible nickel content of any layered oxide cathode and is known to have a severe CALP contraction during the H2 – H3 phase transition.[5,10] For these reasons, LNO serves as an ideal extreme test bed for understanding the impact of electrolytes on the H2 – H3 phase transition. To observe the morphology and composition of the LNO, SEM images were taken along with EDX maps, as shown in Figure 1b. The LNO secondary particles have a relatively spherical shape with a diameter of approximately ~ 10 µm. The EDX maps show a homogenous distribution of nickel further implying a pure $LiNiO_2$ phase was formed. The associated EDX spectrum is presented in Figure S2. The SEM and XRD data together imply that the material is indeed single phase.

We employed five different electrolytes, one of which is a standard baseline electrolyte, while the other four were the same or of similar composition to electrolytes that have been shown to improve cyclability and/or reduce surface reactivity.[20,23,24,26,40] Furthermore, we selected these particular electrolytes because they each used carbonate solvents and $LiPF_6$ salt, which are common in industrial lithium-ion batteries. The molecular structure of all the components used in the electrolytes is shown in Figure 1c, and their specific compositions are summarized in Table 1. The baseline electrolyte, referred to as LP57, is 1 M $LiPF_6$ in a 3 : 7 blend of EC : EMC by weight, with an additional 2% of VC added by weight. The second electrolyte, referred to as F20, is composed of 1.25 M $LiPF_6$ in a 2 : 8 blend of FEC : EMC by weight. The third electrolyte, referred to as F20-P, is composed of the same composition as F20, but with 1% of PFO added by weight. The fourth electrolyte, referred to as LSE-O, is composed of 3 M $LiPF_6$ in a 3 : 7 blend of EC : EMC by weight, mixed with twice the volume of TTE, resulting in a final concentration of 1 M $LiPF_6$.

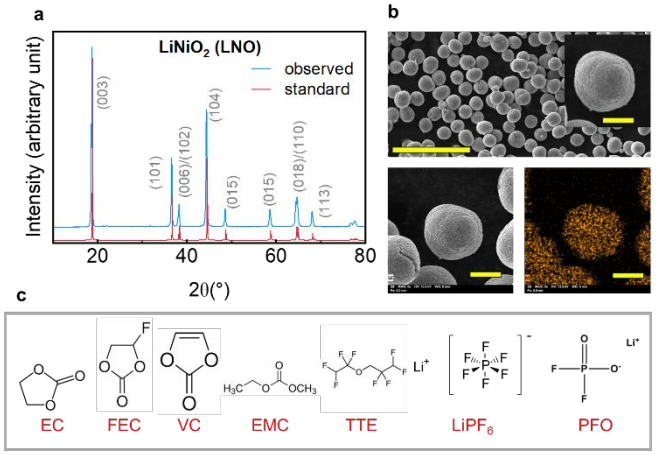

Figure 1(a) XRD pattern of the synthesized LNO with the Miller indices of the prominent peaks labelled, and the reference pattern from Match! Database included. (b) SEM images and EDX maps of LNO. The large scale bar is 50 µm and the small scale bars are 5 µm. (c) Molecular structures of the electrolyte components.

The fifth electrolyte, referred to as LSE-F, is composed of 3 M $LiPF_6$ in a 2 : 8 blend of FEC : EMC by weight, with an 1% PFO by weight, and twice the volume of TTE added, resulting in a final concentration of 1 M $LiPF_6$. Of the four advanced electrolytes used, both F20 and F20-P may be categorized as HFEs, while LSE-O is an example of a traditional LHCE. LSE-F can be viewed as a combination of both an HFE and LHCE.

Table 1 Compositions of the electrolytes

Electrolyte	Composition
LP57	1 M $LiPF_6$ in 3 : 7 EC : EMC (wt.)] + 2 % VC (wt.)
F20	[1.25M $LiPF_6$ in 2 : 8 FEC : EMC (wt.)]
F20-P	1.25 M $LiPF_6$ in 2 : 8 FEC : EMC (wt.)] + 1 % PFO (wt.)
LSE-O	3 M $LiPF_6$ in 3 : 7 EC : EMC (wt.)] + 2 x TTE (vol.)
LSE-F	3 M $LiPF_6$ in 2 : 8 FEC : EMC (wt.) + 1 % PFO (wt.)] + 2 x TTE (vol.)

After preparing the electrolytes, we sought to better understand their physical properties, including oxidative stability, solvation structures, conductivities, and solvation energies. We began by performing LSV on each electrolyte. As shown in Figure 2a, LP57 decomposes rapidly well below 5 V. This is likely due to the poor oxidative stability of the VC additive.[41] Relative to LP57 though, all of the advanced electrolytes show superior oxidative stability, with only slight decomposition of each electrolyte below 5 V. While LSV does give useful insights regarding the relative oxidative stabilities of the electrolytes, it should be noted that LSV tests are performed in blocking conditions with nonreactive counter electrodes. In a cell with reactive electrodes, electrolyte decomposition can be influenced by interactions with the electrodes, i.e., to say that in the cells cycled in this study, we cannot assume that no electrolyte decomposition has occurred below the decomposition voltages seen in the LSV test.

After testing the oxidative stabilities of the electrolytes, we sought to better understand their solvation structures. To do this, we gathered FTIR spectra from each electrolyte, which is presented in Figure S3. By observing the stretching of the P-F bond of the PF_6^- anion, we can make relative comparisons regarding the presence of solvent separated ion pairs (SSIPs) vs. contact ion pair (CIPs).[24] A PF_6^- that is coordinated, with a characteristic FTIR peak at ~ 820 cm^{-1}, implies a more saturated solvation structure while uncoordinated PF_6^-, with a characteristic FTIR peak at ~ 840 cm^{-1}, is indicative of a lower concentration, non-saturated solvation structure.[24] As can be seen in Figure 2b, LP57, F20, and F20-P all have strong peaks in the uncoordinated PF_6^- region. This is expected as their total salt concentration is no greater than 1.25 M, and all the solvents used are known to effectively dissolve $LiPF_6$. Conversely, LSE-O and LSE-F both show a notable peak shift towards the coordinated PF_6^- region. Of note also is that TTE has a strong characteristic FTIR peak in the same region of interest.[24] To remove this overlap, both LSE-O and LSE-F were prepared without the addition of TTE. The FTIR spectra from both LSE-O and LSE-F without TTE labeled, respectively, as SE-O and SE-F, are shown in Figure 2b. Even with the TTE removed, we observe a peak shift towards the uncoordinated PF_6^- region. This is expected, as while the total $LiPF_6$ concentration in these electrolytes remains 1 M with the addition of the TTE, the TTE diluent does not significantly participate in the dissolution of $LiPF_6$ salt.[41,42] This effectively preserves the high concentration solvation structure resulting in an increase in CIPs within the electrolytes. Increased CIP concentration in electrolytes has been shown to improve lithium-metal anode performance,

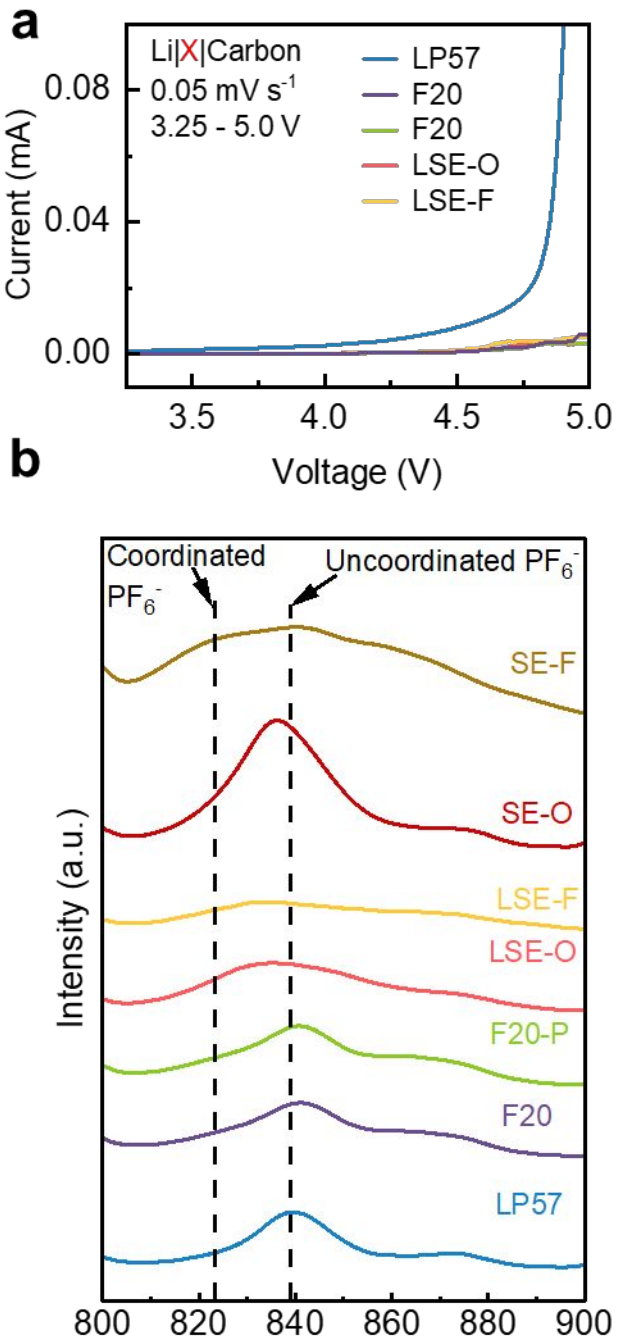

Figure 2 (a) LSV of the various electrolytes. (b) FTIR spectra zoomed on the coordinated and uncoordinated PF_6^- region.

reduce free solvent available for side reactions, and improve the oxidative stability, at the expense of conductivity.[41,43]

To observe this effect more directly, we measured the ionic conductivities of each electrolyte. As seen in Table 2, LP57, F20, and F20-P have conductivities greater than 7 mS cm^{-1}. This is expected as each of these electrolytes has a non-saturated solvation structure dominated by SSIPs, with relatively few CIPs. Notably, the addition of PFO does appear to slightly lower the conductivity of F20-P relative to F20, likely due to the PFO reducing the amount of free solvent. LSE-O and LSE-F, however, show much lower conductivities with each having a conductivity of < 3 mS cm^{-1}. This is consistent with the FTIR measurements, showing that these electrolytes have solvation structures with more CIPs, which are known to lead to reduced conductivity.[43]

Table 2 Measured ionic conductivities of the electrolytes

Electrolyte	Conductivity (mS cm^{-2})
LP57	9.5
F20	9.4
F20-P	7.7
LSE-O	2.3
LSE-F	1.3

In addition to conductivity, solvation structure and composition can influence the solvation energy of electrolytes. Relative solvation energy can be gauged by measuring the voltage upshift of the Li/Li^+ redox couple using a Fc/Fc^+ internal standard.[38,39] Fc/Fc^+ has been shown to vary only minimally with different electrolyte compositions, making it an ideal internal standard. [44] The apparent shift in Fc/Fc^+ observed in the CV tests can, therefore, be attributed to a shift in the Li/Li^+ potential.[39] Greater upshifts in the voltage of Li/Li^+ correlate to more weakly solvating electrolytes. [38,39,45] To test this, we prepared each electrolyte with an additional ~ 10 mM of Fc, which has been shown to not significantly alter the solvation structures.[39] We then conducted CV with each electrolyte in a Li || Ni-foil cell and measured the apparent shift in the Fc/Fc^+ redox couple. The results of these tests are summarized in Table 3 with the CV curves presented in Figure S4. Interestingly, all the electrolytes tested, including LP57, shift the Li/Li^+ potential up from the formal aqueous potential of -3.04 V. Also, of note is that all four advanced electrolytes are more weakly solvating than the baseline LP57. F20 and F20-P have only a small upshift relative to LP57, likely caused by the slightly higher salt concentrations and the incorporation of FEC.[45] LSE-O and LSE-F on the other hand, have much larger upshifts of more than 150 mV relative to LP57, likely due to their more saturated solvation structures, as well as the incorporation of the TTE diluent.[19,45] In the case of LSE-F, the incorporation of FEC also plays a role in increasing the upshift of Li/Li^+ even more so than in LSE-O.

Table 3 Measured upshift of Li/Li^+ potential vs. Fc/Fc^+ and Standard Hydrogen Electrode (SHE)

Electrolyte	Fc/Fc^+ vs. Li/Li^+ (V)	Li/Li^+ vs. SHE (V)
LP57	3.22	-2.58
F20	3.19	-2.55
F20-P	3.19	-2.55
LSE-O	3.05	-2.41
LSE-F	2.99	-2.35
Aqueous	3.68	-3.04

Having characterized the individual electrolytes, we sought to directly test their influence on the reversibility of the H2 – H3 phase transition. To do this the LNO powder was cast into electrodes, which were then placed in Li-metal half-cells filled with the electrolyte of interest. The cells were then cycled for three C/10 formation cycles, followed by 100 cycles at C/3 rate. The voltage curves of the third formation cycle for each electrolyte are shown in Figure 3a. LNO in each electrolyte gives a third cycle C/10 discharge capacity of ~ 230 mA h g^{-1}. Of note also is that the H2 – H3 phase transition plateaus, seen at ~ 4.1 – 4.3 V, are present with each sample, and of roughly the same initial length and flatness. To further verify the occurrence of the H2 – H3 phase transition, we performed dQ dV^{-1} analysis on the third formation cycle voltage curves, as seen in Figure 3b. The peaks associated with the H2 – H3 phase transition at ~ 4.1 – 4.3 V are clearly visible with comparable peak widths and intensities seen with each electrolyte. This implies that no significantly different degradation has taken place in the H2 – H3 region for any of the electrolytes before cycling. To further confirm the occurrence of the H2 – H3 phase transition, we performed ex situ XRD on charged LNO electrodes at 4.1 and 4.4 V. The collected patterns are shown in Figure S5. At 4.1 V, the leftward shift of the (003) peak signifying c-axis lattice parameter expansion is expected as the material is in the H2 phase at this point. In the pattern taken at 4.4 V, the shift in the (003) peak to higher 2θ values, relative to the pattern taken at 4.1 V, is indicative of the c-axis lattice parameter contraction expected in the H2 – H3 phase transition. Interestingly, the peak splitting in the 4.4 V pattern, seen in the (003) and (104) peaks, implies that the H2 – H3 phase transition is not complete yet in LNO at 4.4 V. This data agrees well with the dQ dV^{-1} analysis and further shows that the LNO is experiencing the H2 – H3 phase transition at the expected voltages. Of note is that all of the patterns in Figure S5 were collected with electrodes, which explains the additional peak associated with the aluminum foil, seen at ~ 66˚.

After the formation cycles, all the cells were cycled galvanostatically for 100 cycles at a C/3 rate. The discharge capacities, along with the percent of the initial C/3 capacity, of these cells are shown in Figure 3c. Unsurprisingly, LP57 loses the most capacity while cycling, followed, respectively, by LSE-O, F20, LSE-F and F20-P. Of note is that both electrolytes with the PFO additive cycle most stably, and that the three best

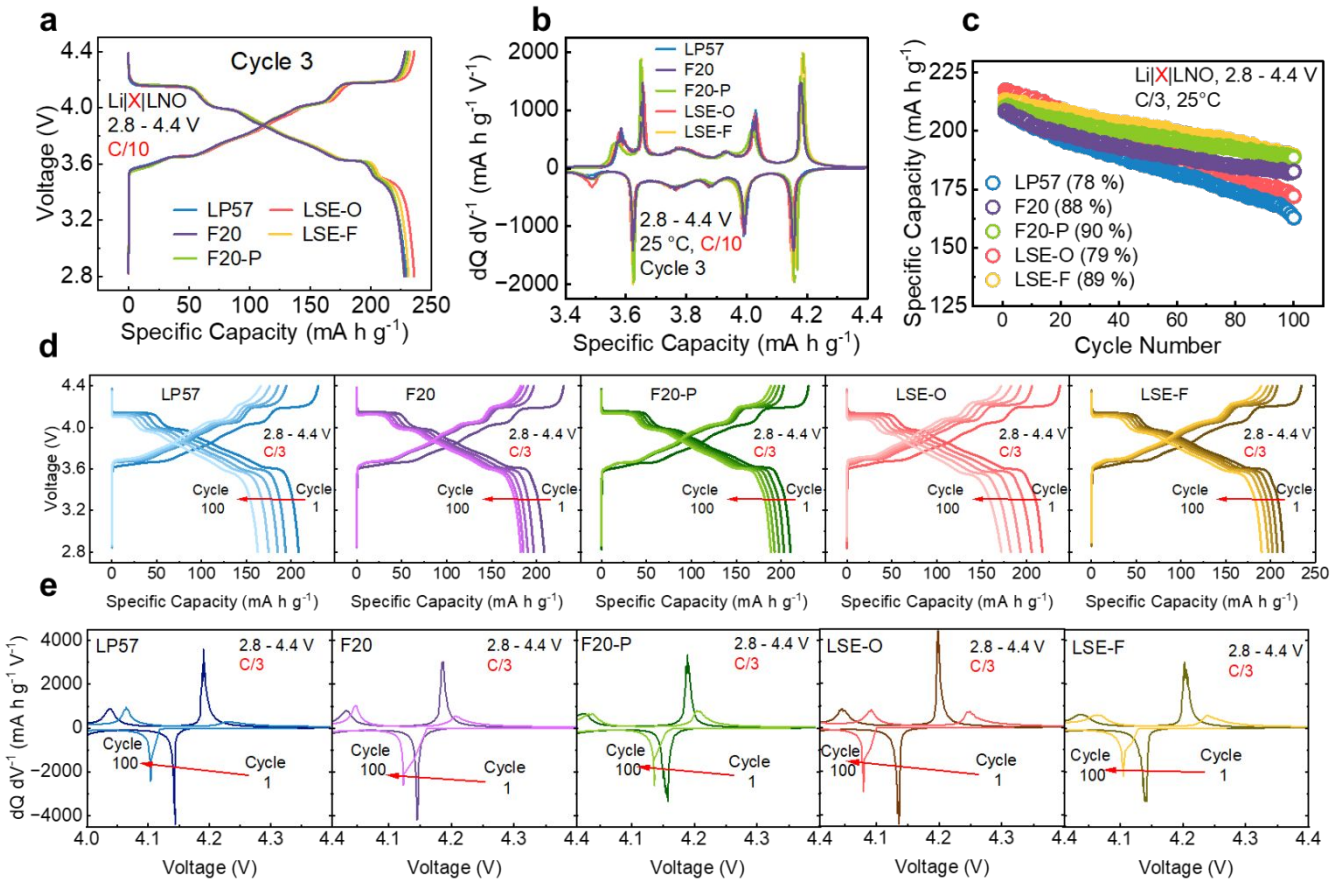

Figure 3 (a) Third formation cycle voltage curves. (b) dQ dV^{-1} analysis of third formation cycle. (c) Galvanostatic specific discharge capacity at a C/3 rate. (d) Voltage curves taken every 25th cycle the course of cycling. (e) dQ dV^{-1} analysis of the first and 100th C/3 cycles zoomed in on the H2 – H3 phase transition region.

electrolytes all contain FEC. Furthermore, F20 and F20-P were only slightly more weakly solvating than LP57, unlike LSE-O and LSE-F. This implies that while solvation energy is a good indicator of Li-metal anode performance, it does not strongly correlate with the ability of an electrolyte to improve the galvanostatic cycling of LNO.[38,45]

To further delve into the effects of each electrolyte on the H2 – H3 phase transition, we plotted both the charge and discharge voltage curves every 25 cycles as shown in Figure 3d. In every case, the H2 – H3 charge plateau becomes shorter and steeper with progressive cycling. This is likely caused by both the H2 – H3 phase transition becoming more kinetically hindered, and active material loss.[32] The H2 – H3 discharge plateaus also shorten with cycling, further reflecting the continued degradation of the phase transition in all electrolytes with cycling. Again, here we can see that the HFEs - F20, F20-P, and LSE-F - all appear to suffer less degradation than the FEC-free LSE-O and LP57. LSE-O though does appear to positively affect the H2 – H3 reversibility, with the 100th cycle charge curve of LSE-O being notably flatter and less steep than that of LP57 in the H2 – H3 region.

To qualitatively observe the degree of degradation of the H2 – H3 phase transition, we performed dQ dV-1 analysis on both the first and final C/3 cycle, with the full plots shown in Figure S6 and a zoomed-in view of the H2 – H3 phase transition region presented in Figure 3e. While the LNO in each electrolyte has strong peaks in the H2 – H3 phase transition region in the first cycle, by the 100th cycle, the same peaks reduce significantly in intensity. The charge peaks in particular shrink and broaden by the 100th cycle. While the trend of degradation is universal in all electrolytes, the shapes of the 100th cycle dQ dV-1 plots indicate that the degradation in the H2 – H3 phase transition region is not uniform across all the electrolytes. Specifically, the 100th cycle charge peaks in each of the four advanced electrolytes appear to be sharper and less broad than the 100th cycle charge peak in LP57. This implies that the H2 – H3 phase transition is less kinetically hindered in the advanced electrolytes than in the baseline LP57.[7,32] Also of note is that the rightward shift of the peaks on charge, and the leftward shift on discharge, indicative of cell polarization, are most prominent in the EC-containing LP57, and LSE-O. LSE-O in particular appears to have the largest cell polarization of all the electrolytes, despite better retaining the H2 – H3 phase transition peak in the 100th cycle. This increased cell polarization may explain why LSE-O cycles only marginally better than the LP57 despite maintaining the H2 – H3 phase transition better. Conversely, the HFEs show notably less cell polarization. These trends hint that the use of both saturated solvation structures and fluorinated solvents are viable strategies to improve the reversible accessibility of the H2 – H3 phase transition. However, it would appear that the use of fluorinated solvents is a more effective strategy, among the electrolytes tested.

HFEs providing superior surface stabilization is understandable, since to reconstruct the surface of LNO, Ni^{4+} must be reduced to Ni^{2+} to ultimately form a rock-salt like phase.[6] This requires that another species be oxidized. While there are various potential ways for this to happen, one likely path is for the organic solvents to be oxidized. From the trends seen in our study, it appears that EC is more easily oxidized than FEC. This makes a degree of sense, since in FEC the inclusion of the highly electronegative fluoride will pull electron density away from the double bonded coordinating oxygen. This lower electron density on the ligand coordinated to Li^+ would make the oxidation of FEC less likely than the oxidation of EC. Naturally, this would lead to less reduction of Ni^{4+} on the LNO surface, resulting in less surface reconstruction in the FEC containing electrolytes. Indeed, calculations have shown that FEC is more easily reduced, and therefore less easily oxidized, than EC. [46] LSE-O outperforms LP57 likely due to the fact that LSE-O has far less free solvent than LP57. Free solvent can be more easily reacted than solvent coordinated to Li^+.

While dQ dV^{-1} is helpful for relative comparisons, it does not allow for easy quantitative comparisons of the H2 – H3 phase transition discharge capacity. To do this, we turned to 2nd derivative analysis (SDA), a technique used in other branches of research, but as of yet not applied to look at electrochemically driven phase transitions in layered oxide cathodes. [47,48] SDA makes it possible to define the onset and end points of phase transitions by identifying inflection points in a voltage curve (Q(V)), as shown in Figure 4a. These inflection points correspond to local minima and maxima in the first derivative of Q(V), which is the well-known dQ dV^{-1}, as shown in Figure 4b and eq 1. In the second derivative (d^2Q dV^{-2}), these inflection points become zeros, allowing us to easily identify the voltage range over which a phase transition of interest takes place, as shown in Figure 4c and eq 2. It should be noted that these endpoints do not indicate that the phase transition is fully complete in every single particle in the electrode. Rather, since the measured voltage reflects the average potential across the electrode, the endpoints found in SDA give the range over which the phase transition is the dominant electrochemical reaction within the vast majority of the electrode. Small pockets of material within the electrode may be at a different state of charge (SOC), and therefore a different phase, but their impact on the voltage curve is small enough, as to not greatly affect the voltage reading.

$$d/dV\ Q(V) = dQ/dV \qquad \text{eq 1.}$$

$$d^2/dV^2\ Q(V) = d^2Q/dV^2 \qquad \text{eq 2.}$$

To quantify the reversible capacity retention through the H2 – H3 phase transition, we performed SDA on every 10th cycle for cells cycled with each electrolyte. Additionally, we performed the same analysis for the M – H2 phase transition region. The results of this analysis are summarized in Figure 4d-e. Of interesting note is that on charge, the LNO does not reach the end inflection point of the H2 – H3 phase transition by 4.4 V. This implies that while the H2 – H3 plateau has ended by 4.4 V, LNO is still undergoing the H2 – H3 phase transition. Consistent with the voltage curve and dQ dV^{-1} analysis seen in Figure 3, the discharge capacity of the H2 – H3 phase transition decreases with cycling in all electrolytes. LP57 has the worst retention, followed by LSE-O, F20, LSE-F, and F20-P. In every case, the M – H2 discharge capacity retention is superior for each electrolyte, compared to its H2 – H3 capacity retention. While each advanced electrolyte outperforms LP57, the degree to which they outperform is not the same as seen in the total C/3

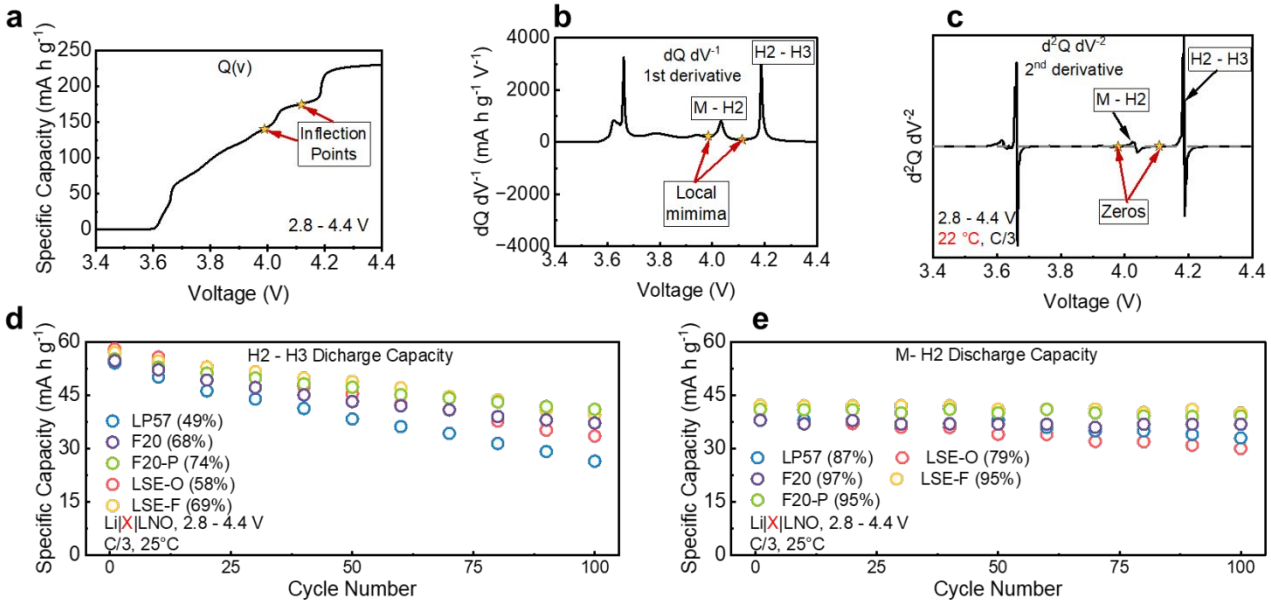

Figure 4 (a) An example voltage curve showing a typical Q(V) curve, with the M - H2 phase transition beginning and end inflection points highlighted. (b) An example dQ dV^{-1} curve, derived from the example Q(V) curve, with the M – H2 phase transition local minima highlighted. (c) Example d^2Q dV^{-2}, derived from the example Q(V) curve, with the M – H2 phase transition zeros highlighted. (d) Discharge specific capacity of the H2 – H3 phase transition with every 10th cycle plotted. (e) Discharge specific capacity of the M – H2 phase transition with every 10th cycle plotted.

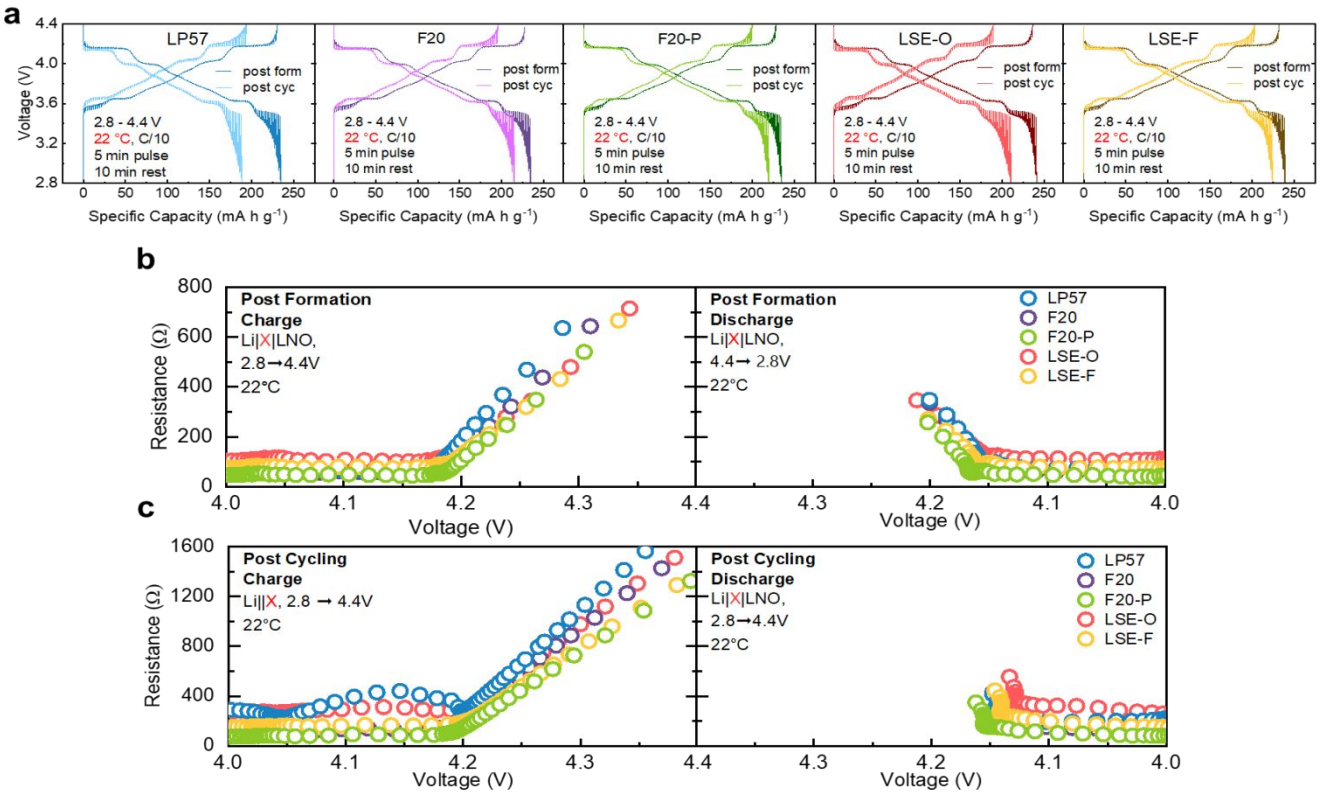

Figure 5 (a) Pre and post cycling GITT charge and discharge curves. (b) Calculated resistances in the H2 – H3 voltage region after formation cycles. (c) Calculated resistances in the H2 – H3 voltage region after 100 C/3 cycles.

cycling, seen in Figure 3c. Furthermore, when compared to the discharge capacity in the H2 – M phase transition region, it appears that the H2 – M and H2 – H3 regions have different degrees of capacity fade. The difference in the degree of capacity fade between the two regions could be related to the material being able to undergo the H2 – H3 phase transition to a lesser extent, but otherwise being electrochemically active through the rest of the possible phase transitions. Effects such as a surface pinning rock-salt layer can cause such degradation, by limiting the CALP contraction necessary to undergo the H2 – H3 phase transition.[49] Furthermore, polarization may make the H2 – H3 phase transition inaccessible as its kinetics degrade with cycling and/or overall cell polarization grows.

To probe how the kinetics of the H2 – H3 phase transition changes with cycling in each electrolyte, we turned to GITT. GITT allows for the observation of the overpotential, and resistance at many points across the entire voltage range of the cell.[10] By comparing the resistances experienced when passing through the H2 – H3 phase transition before and after cycling, we can glean insights into the evolution of the kinetics of the H2 – H3 phase transition. To that end, we conducted GITT tests in each electrolyte immediately after the formation cycles, and after cycling for 100 cycles at C/3 rate. The voltage curves from these tests are shown in Figure 5a. Qualitatively, it can be seen that each electrolyte has roughly the same overpotential when charging through the H2 – H3 phase transition during the post formation charge. This is further reflected in the calculated resistance values from 4 – 4.4 V presented in Figure 5b. However, after cycling, there appears to be greater resistance when charging through the H2 – H3 phase transition in the LP57 and LSE-O electrolytes than in the HFEs, as seen in Figure 5c. The PFO-containing F20-P and LSE-F notably have even lower resistance values than the PFO-free F20. Upon discharge, the resistances shrink in each electrolyte, likely due to the superior discharge kinetics of the H2 – H3 phase transition relative to charge.[10] From this analysis, it appears that the all the advanced electrolytes do reduce the resistance when charging through the H2 – H3 phase transition. However, again we see that using fluorinated solvents and the PFO additive seem to lead to lower degrees of resistance increase in the H2 – H3 phase transition region.

In addition to providing insight to the cell-level resistance, GITT also allows for the minimization of overpotential effects, and by extension the isolation of the thermodynamic voltage curves by plotting the data points at the end of each rest step.[10,50] Thermodynamic voltage curves can be used to minimize the effects of kinetic hinderances on capacity fade. By doing this, we can separate the apparent fade caused by kinetic limitations from the fade caused by true active material loss, i.e., thermodynamic fade.[50] Coupled with SDA, the thermodynamic curves can provide insight into the true state of the H2 – H3 phase transition before and after cycling. To this end, we extracted and plotted the thermodynamic voltage curves as seen in Figure S7. We then performed SDA on each

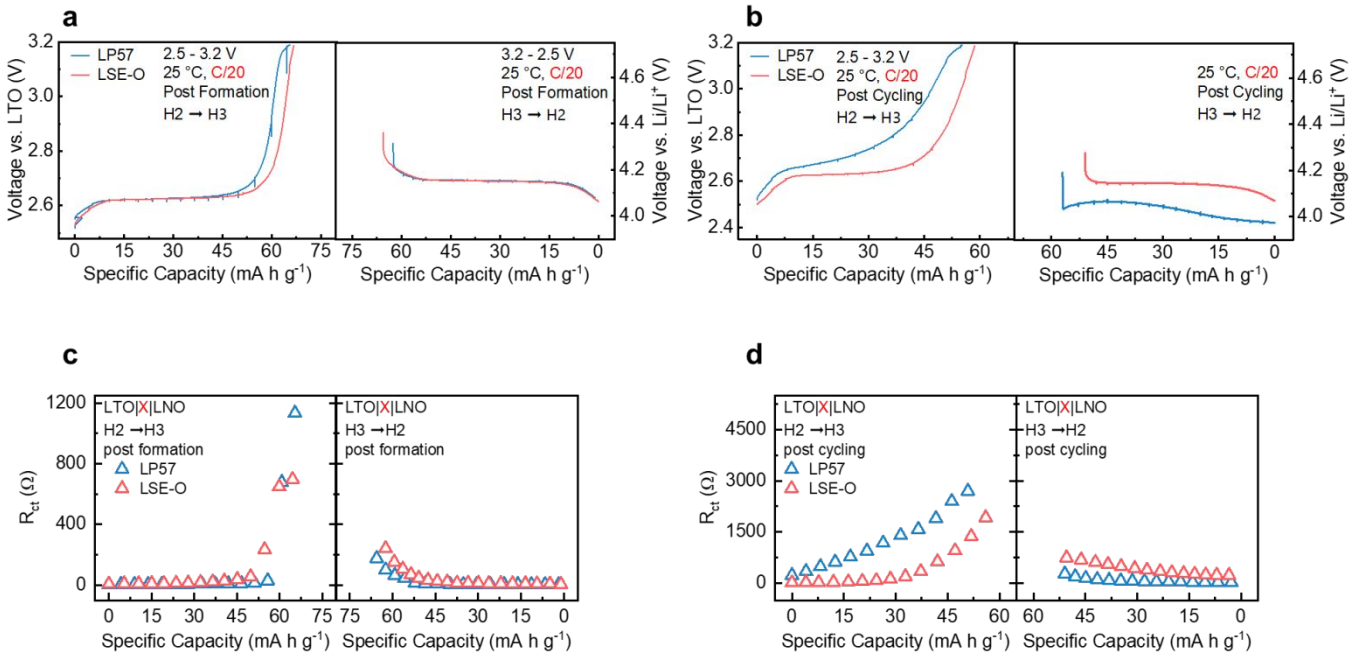

Figure 6 (a) Charge and discharge curves seen in GEIS testing after the formation cycles. (b) Charge and discharge curves seen in GEIS testing after 100 C/3 cycles. (c) Fitted R_{ct} values during GEIS testing after the formation cycles. (d) Fitted R_{ct} values during GEIS testing after 100 C/3 cycles.

discharge curve and plotted their capacities in Figure S8. We see that the baseline LP57 experiences the most thermodynamic fade, with a capacity retention (65%) followed by LSE-O (74%). Of surprising note though is that all of the HFEs have virtually the same capacity retention in the H2 – H3 phase transition region (85%). This stands in contrast to the C/3 cycling data, seen in Figure 3. This implies that while each of the HFEs induces different amounts of overpotential, resulting in varying H2 – H3 phase transition kinetics, their abilities to stabilize the cathode surface and influence the thermodynamic reversibility of the H2 – H3 phase transition are virtually identical over the tested cycling period.

While GITT is certainly useful in understanding the resistance seen in the cell, it requires that the system be at rest to obtain a resistance measurement. This limits the ability of the technique to measure resistance dynamically. Furthermore, GITT does not allow for the deconvolution of the various sources of impedance in a cell, i.e., charge-transfer resistance (R_{ct}) vs. contact resistance ($R_{contact}$). However, GEIS does allow for the deconvolution of impedance and requires no rest step in order to take its measurements. For these measurements to be accurate, we needed a stable anode that would have a negligible impedance change during the measurements and over the course of cycling. Li-metal was too reactive to be a suitable anode. However, LTO is known to be highly stable and form little to no solid-electrolyte interphase (SEI) with standard electrolytes.[51] The flat voltage profile of LTO, at ~ 1.55 V vs. Li/Li^+, also makes it ideal for GEIS, as voltage shifts can be solely attributed to changes in the cathode.[51] Furthermore, we previously used LTO successfully in similar GEIS tests.10 We therefore proceeded to build LTO || LNO cells with each electrolyte. We then conducted GEIS measurements after the formation cycles and after 100 cycles at C/3 rate. The cycling performance of the LTO cells is shown in Figure S9. We found in our cycling that the FEC-containing electrolytes cycled more poorly than expected. We attribute this to the FEC forming a thick SEI on the LTO anode, as has been previously reported.49 With this in mind, while we did take GEIS measurements with them, we have excluded the HFEs from this analysis as we were unable to confidently assume that the LTO had a negligible contribution to impedance growth.

To analyze the GEIS data, we first confirmed that the cells had undergone the H2 – H3 phase transition. As can be seen in Figure 6a after the initial formation, the typical flat plateau at ~ 4.1 V vs. Li/Li^+ is present for both the LP57 and LSE-O samples during both charge and discharge. However, after 100 cycles, the charge voltage curve of the LP57 cells shifted up significantly, and no longer shows a flat voltage plateau, but rather a highly sloped curve through the H2 – H3 phase transition, as seen in Figure 6b. A similar trend is seen on discharge with the LP57 discharge voltage curve after cycling being shifted down significantly, and only undergoing the H2 – H3 phase transition fully after reaching below 4 V vs. Li/Li^+. The charge and discharge curves of LP57 imply a significant increase in the impedance in the H2 – H3 region has occurred, which hinders the ability of the material to undergo the phase transition. On the other hand, the LSE-O samples show much less degradation in their voltage profiles between pre- and post-cycling tests. Specifically, LSE-O appears to have relatively minimal degradation in the H2 – H3 charge plateau after cycling, with the plateau sloping up only slightly towards the end. Furthermore, the LSE-O post cycling discharge plateau remains flat with no significant shift in overpotential between pre- and post-cycling.

Having confirmed that both samples had undergone the H2 – H3 phase transition, we proceeded to model the GEIS data

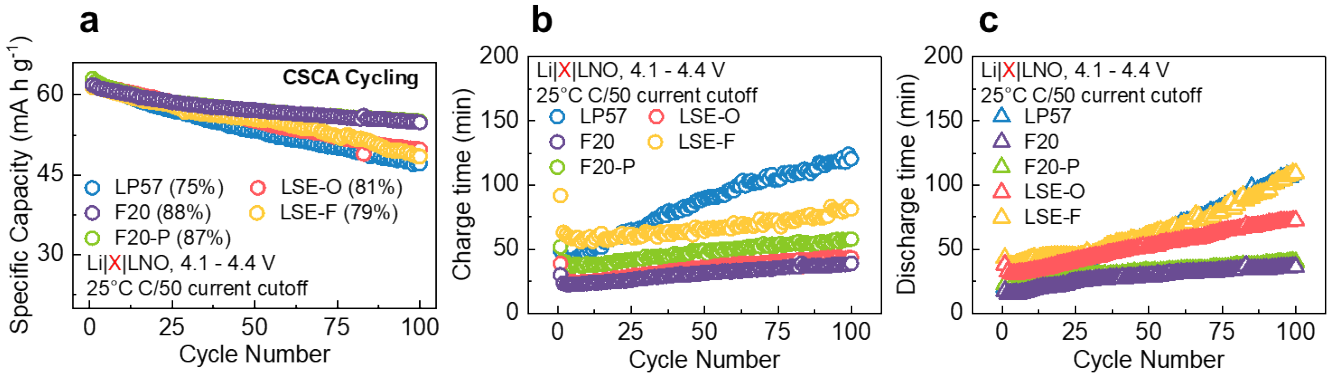

Figure 7 (a) Specific discharge capacities obtained during CSCA cycling. (b) Charge times observed during CSCA cycling. (c) Discharge times observed during CSCA cycling.

using equivalent-circuit analysis. The equivalent circuit used is shown in Figure S10 and the collected GEIS curves are shown in Figure S11. We found that both R_S, which we attribute to the resistance of the testing equipment, and $R_{contact}$ varied negligibly during our tests. However, R_{ct} did vary significantly during testing. The fitted R_{ct} values are presented in Figure 6c-d. Like the voltage curves, the R_{ct} values of both the LP57 and LSE samples evolve very similarly to one another when tested after the formation cycles. However, after cycling, the LP57 samples experience significantly higher R_{ct} than the LSE-O samples, along with a greater R_{ct} increase over the course of charge. This coupled with the increased overpotential seen on both charge and discharge, implies that the surface degradation seen in the LP57 samples has significantly hindered the ability of the LNO to undergo the H2 – H3 phase transition. Furthermore, the relatively lower R_{ct} values seen in the LSE-O samples during charge after cycling, along with the better maintained voltage curves imply that the lower amount of surface reconstruction seen with LSE-O allows for a more facile H2 – H3 phase transition. This makes a degree of logical sense, since electrochemical phase transitions in layered oxide cathodes are known to initiate at the particle surface and proceed to nucleate into the bulk.35 Excessive surface reconstruction likely hinders both the initiation as well as the nucleation of the phase transition, requiring higher overpotentials in order to drive the phase transition reaction, as seen in LP57.46 While we were unfortunately not able to perform the same GEIS analysis with all electrolytes, due the incompatibility of FEC and LTO, it is likely the HFEs would exhibit even lower R_{ct} growth than LSE-O based on the galvanostatic cycling and GITT tests.

Having examined both the static and dynamic evolution of impedance in the cells with different electrolytes, we sought to understand how the rate capabilities of each electrolyte in the H2 – H3 region would evolve with cycling. To do this, we employed potentiostatic cycling, which is alternatively known as cyclic step chronoamperometry (CSCA). CSCA has distinct advantages over traditional galvanostatic rate tests because it is able to induce a wide range of rates over a single cycle and ensures that the material is always at its maximum rate for a given SOC within a specified cutoff voltage window.50 For these tests, Li-metal half cells with an LNO cathode were cycled potentiostatically in each of the 5 electrolytes at 4.1 – 4.4 V, until reaching a cutoff current of C/50. The discharge capacities are presented in Figure 7a. F20 provides the best capacity retention, followed closely by F20-P, and then surprisingly LSE-O, LSE-F, and LP57. In this case, it is likely that the lower conductivities of LSE-O and notably LSE-F hinder their ability to transport Li^+ ions as rapidly or as facilely as the less concentrated F20 and F20-P electrolytes. This can be seen in the charge and discharge times plotted in Figure 7b-c. While LP57 has the largest increase in both charge and discharge times over the course of cycling, the low conductivity LSE-F has the second largest increase in both the charge and discharge times. LSE-O has less increase in its discharge times than LSE-F, while F20 and F20-P, which both have conductivities of greater than 7 mS cm^{-1}, show a relatively minor increase in their charge and discharge times.

Examining the c-rate vs. capacity plots of charge and discharge, presented in Figure S12, sheds further light on the sources of the CSCA cycling performance. Surprisingly, it appears that the maximum rate for each electrolyte is achieved on charge, which is likely due to the expanded Li^+ diffusion channels of the H2 phase.10,29 The lower maximum rates seen during discharge are likely due to the Li^+ having to initially intercalate into the narrower Li^+ diffusion channels of the H3 phase.10,29 Furthermore, it appears that LP57 experiences severe decay in its rate capability when passing through the H2 – H3 phase transition, as seen in Figure S12a. The excellent conductivity of LP57 allows it to deliver a high initial maximum rate of 24.5C during the 3rd cycle charge. Due to its apparent inability to effectively passivate the LNO surface though by the 100th CSCA cycle, LNO in LP57 can only charge at a maximum rate of 5.5C, which represents a 78% drop in maximum rate capability from the 3rd cycle. This stands in stark contrast to the rate capabilities of F20 and F20-P, which have maximum charge rates during their 3rd cycles of, respectively, 31.8C and 12.6C, as seen in Figure S12b-c. F20 and F20-P notably experience less relative loss in rate capability compared with LP57, with F20 and F20-P having maximum 100th cycle rates of, respectively 10.6C and 4.9C. This shows that F20 and F20-P experience, respectively, a 67% and a 61% loss in maximum rate capability between the 3rd and 100th CSCA charge cycles. In regard to the LHCEs, despite their good performance in galvanostatic tests, LSE-F and LSE-O can only deliver maximum third cycle charge

rates of, respectively, 6C and 12.4C, as shown in Figure S12d-e. The maximum charge rates of the LSE-F and LSE-O samples further decay to, respectively, 1.1C and 5.4C during the 100th CSCA cycle charge. This means that LSE-F experiences the largest relative rate capability decrease between the 3rd and 100th CSCA charge cycles of all the electrolytes tested, with an 82% loss in maximum rate. LSE-O, however, only loses 56% of its maximum charge rate capability, which is the best relative rate retention of all the electrolytes tested. However, the inability of LSE-O to passivate the LNO surface, comparably to the FEC-containing electrolytes likely explains its inferior capacity retention compared with F20 and F20-P in the CSCA cycling tests. From the CSCA tests it appears that a combination of surface stabilization and conductivity are needed to stabilize the high rate performance of the H2 – H3 phase transition.

Conclusions

In conclusion we observed that each of the advanced electrolytes does improve the galvanostatic cyclability of LNO, with the PFO-containing electrolytes performing the best. From dQ dV^{-1} analysis, we saw qualitatively that each of the advanced electrolytes improves the reversibility of the H2 – H3 phase transition. We further found quantitively with SDA that the reversibility of the H2 – H3 phase transition is not only improved with advanced electrolytes, but the degree of capacity fade is different in different phase transition regions. The larger fade in the H2 – H3 phase transition is due to surface reconstruction and polarization growth limiting accessibility to the phase transition. With GITT, we observed that the fluorinated solvents and the PFO additive lead to lower amounts of resistance growth in the H2 – H3 phase transition region with cycling. From the thermodynamic GITT and SDA, we quantitatively estimated the thermodynamic capacity retention in the H2 – H3 region. In this analysis, we found again that the HFEs better maintained the reversibility of the H2 – H3 phase transition. Surprisingly, despite showing different degrees of capacity loss under galvanostatic cycling conditions, each of the HFEs had virtually identical degrees of relative thermodynamic fade. This implied that the inherent impedance growth caused by these electrolytes lead to the observed differences in their galvanostatic H2 – H3 phase transition capacity retention. GEIS data further showed that the use of advanced electrolytes can greatly reduce the increase in R_{ct} with cycling, thus improving the kinetics of the H2 – H3 phase transition. We attributed this to reduced surface reconstruction on the LNO particle surface, resulting in both a more facile initiation and subsequent nucleation of the H2 – H3 phase transition. Lastly, CSCA demonstrated that a combination of surface stabilization as well as conductivity are needed to preserve the high rate performance of the H2 – H3 phase transition with lower concentration HFEs giving the best capacity retention and relative rate retention after cycling. Overall, the application of advanced electrolytes can significantly impact the reversibility of the H2 – H3 phase transition in high-Ni cathodes, with fluorinated solvents and the PFO additive being the most effective of the advanced electrolyte investigated in this study.

Author Contributions

J.B.A designed and carried out the experiments. Both authors wrote the manuscript. A.M. supervised the work.

Conflicts of interest

The corresponding author (A.M.) is a co-founder of TexPower EV Technologies, a company focusing on cobalt-free cathode materials for lithium-based batteries.

Acknowledgements

This work was supported by the Assistant Secretary for Energy Efficiency and Renewable Energy, Office of Vehicle Technologies of the U.S. Department of Energy, through Advanced Battery Materials Research (BMR) Program (Battery500 Consortium) Grant DE-AC05-76RLO1830 and Welch Foundation Grant F-1254.

References

1 1 W. Li, E. M. Erickson and A. Manthiram, *Nat Energy*, 2020, **5**, 26–34.
2 2 A. Manthiram, *Nat Commun*, 2020, **11**, 1550.
3 3 K. Mizushima, P. C. Jones, P. J. Wiseman and J. B. Goodenough, *Mater Res Bull*, 1980, **15**, 783–789.
4 4 A. Manthiram and J. B. Goodenough, *Nat Energy*, 2021, **6**, 323–323.
5 5 M. Bianchini, M. Roca-Ayats, P. Hartmann, T. Brezesinski and J. Janek, *Angewandte Chemie - International Edition*, 2019, 58, 10434–10458.
6 6 Z. Cui, Z. Guo and A. Manthiram, *Adv Energy Mater*, DOI:10.1002/aenm.202203853.
7 7 N. Zhang, S. Yu, I. Hamam, B. Tang, M. Johnson and J. R. Dahn, *J Electrochem Soc*, 2024, **171**, 010520.
8 8 P. Vanaphuti, Z. Cui and A. Manthiram, *Adv Funct Mater*, DOI:10.1002/adfm.202308619.
9 9 C. Liu, Z. Cui and A. Manthiram, *Adv Energy Mater*, DOI:10.1002/aenm.202302722.
10 10 J. B. Adamo and A. Manthiram, DOI:10.1021/acs.chemmater.4c01033.
11 11 F. Wang and J. Bai, *Batter Supercaps*, 2022, 5.
12 12 M. Ge, S. Wi, X. Liu, J. Bai, S. Ehrlich, D. Lu, W. K. Lee, Z. Chen and F. Wang, *Angewandte Chemie - International Edition*, 2021, **60**, 17350–17355.
13 13 S. Lee, L. Su, A. Mesnier, Z. Cui and A. Manthiram, *Joule*, 2023, **7**, 2430–2444.
14 14 B. Dong, A. D. Poletayev, J. P. Cottom, J. Castells-Gil, B. F. Spencer, C. Li, P. Zhu, Y. Chen, J. M. Price, L. L. Driscoll, P. K. Allan, E. Kendrick, M. S. Islam and P. R. Slater, *J Mater Chem A Mater*, 2024, **12**, 11390–11402.
15 15 Z. Bai, Z. Ying, F. Zhang, W. Wang, Z. Huang, T. Yang, W. Li, W. Dong, J. Yan, C. Lin, L. Hu, T. Liu, Z. Lin, T. Li, C. Sun, L. Li, Y. Wang, Q. Kong, S. Gu, H. Shen, S. Hao, X. Chen, L. Y. Frank Lam, X. Hu, H. Huang, X. L. Wang, F. Xie, G. Chen, Q. Liu and Y. Ren, *ACS Energy Lett*, 2024, **9**, 2717–2726.
16 16 R. May, J. C. Hestenes, N. A. Munich and L. E. Marbella, *J Power Sources*, 2023, **553**, 232299.

17 17 S. Chen, J. Zheng, D. Mei, K. S. Han, M. H. Engelhard, W. Zhao, W. Xu, J. Liu and J. Zhang, *Advanced Materials*, 2018, **30**, 1706102.
18 18 J. B. Adamo, L. Su and A. Manthiram, *ACS Appl Mater Interfaces*, DOI:10.1021/acsami.2c22786.
19 19 Z. Guo, Z. Cui, R. Sim and A. Manthiram, *Localized High-Concentration Electrolytes with Low-Cost Diluents Compatible with Both Cobalt-Free LiNiO Cathode and Lithium-Metal Anode*, .
20 20 M. Yi, L. Su and A. Manthiram, *J Mater Chem A Mater*, DOI:10.1039/d3ta01061a.
21 21 X. Fan, X. Ji, L. Chen, J. Chen, T. Deng, F. Han, J. Yue, N. Piao, R. Wang, X. Zhou, X. Xiao, L. Chen and C. Wang, *Nat Energy*, 2019, **4**, 882–890.
22 22 X. Zheng, Z. Gu, X. Liu, Z. Wang, J. Wen, X. Wu, W. Luo and Y. Huang, *Energy Environ Sci*, 2020, **13**, 1788–1798.
23 23 R. Pan, Z. Cui, M. Yi, Q. Xie and A. Manthiram, *Adv Energy Mater*, DOI:10.1002/aenm.202103806.
24 24 L. Su, X. Zhao, M. Yi, H. Charalambous, H. Celio, Y. Liu and A. Manthiram, *Adv Energy Mater*, 2022, **12**, 2201911.
25 25 T. Famprikis, P. Canepa, J. A. Dawson, M. S. Islam and C. Masquelier, *Nat Mater*, 2019, 18, 1278–1291.
26 26 R. Pan, E. Jo, Z. Cui and A. Manthiram, *Adv Funct Mater*, DOI:10.1002/adfm.202211461.
27 27 Y. Ji, P. Zhang, M. Lin, W. Zhao, Z. Zhang, Y. Zhao and Y. Yang, *J Power Sources*, 2017, **359**, 391–399.
28 28 X. Yang, J. Li, L. Xing, Y. Liao, M. Xu, Q. Huang and W. Li, *Electrochim Acta*, 2017, **227**, 24–32.
29 29 Q. Xie, Z. Cui and A. Manthiram, *Advanced Materials*, DOI:10.1002/adma.202100804.
30 30 W. Li, H. Y. Asl, Q. Xie and A. Manthiram, *J Am Chem Soc*, 2019, **141**, 5097–5101.
31 31 R. Sim and A. Manthiram, *Adv Energy Mater*, DOI:10.1002/aenm.202303985.
32 32 J. Li, J. Harlow, N. Stakheiko, N. Zhang, J. Paulsen and J. Dahn, *J Electrochem Soc*, 2018, **165**, A2682–A2695.
33 33 S. Ober, A. Mesnier and A. Manthiram, *ACS Appl Mater Interfaces*, DOI:10.1021/acsami.2c20268.
34 34 W. Che, X. Wan, D. Zhang and C. Chang, *ACS Sustain Chem Eng*, 2021, **9**, 5536–5545.
35 35 S. Jamil, G. Wang, L. Yang, X. Xie, S. Cao, H. Liu, B. Chang and X. Wang, *J Mater Chem A Mater*, 2020, **8**, 21306–21316.
36 36 A. J. Merryweather, C. Schnedermann, Q. Jacquet, C. P. Grey and A. Rao, *Nature*, 2021, **594**, 522–528.
37 37 W. Li, S. Lee and A. Manthiram, *Advanced Materials*, 2020, **32**, 2002718.
38 38 S. Ko, T. Obukata, T. Shimada, N. Takenaka, M. Nakayama, A. Yamada and Y. Yamada, *Nat Energy*, 2022, **7**, 1217–1224.
39 39 P. K. R. Kottam, D. Kalkan, M. Wohlfahrt-Mehrens and M. Marinaro, *J Electrochem Soc*, 2019, **166**, A1574–A1579.
40 40 L. Su, E. Jo and A. Manthiram, *ACS Energy Lett*, 2022, **7**, 2165–2172.
41 41 M. Kubot, L. Balke, J. Scholz, S. Wiemers-Meyer, U. Karst, H. Hayen, H. Hur, M. Winter, J. Kasnatscheew and S. Nowak, *Advanced Science*, DOI:10.1002/advs.202305282.
42 42 L. Su, E. Jo and A. Manthiram, *ACS Energy Lett*, 2022, **7**, 2165–2172.
43 43 K. Dokko, N. Tachikawa, K. Yamauchi, M. Tsuchiya, A. Yamazaki, E. Takashima, J.-W. Park, K. Ueno, S. Seki, N. Serizawa and M. Watanabe, *J Electrochem Soc*, 2013, **160**, A1304–A1310.
44 44 J. W. Diggle, A. J. Parker, P. Delahay, R. N. Adams, R. S. Nicholson, D. Bauer, M. Breant and H. Strehlow, *Chemistry of Non-Aqueous Solvents"; Lagowski*, Academic Press, 1980, vol. 19.
45 45 S. C. Kim, X. Kong, R. A. Vilá, W. Huang, Y. Chen, D. T. Boyle, Z. Yu, H. Wang, Z. Bao, J. Qin and Y. Cui, *J Am Chem Soc*, 2021, **143**, 10301–10308.
46 46 T. Hou, G. Yang, N. N. Rajput, J. Self, S. W. Park, J. Nanda and K. A. Persson, *Nano Energy*, DOI:10.1016/j.nanoen.2019.103881.
47 47 A. Tabak, *International Transactions on Electrical Energy Systems*, DOI:10.1002/2050-7038.13211.
48 48 D. Izci and S. Ekinci, *e-Prime - Advances in Electrical Engineering, Electronics and Energy*, DOI:10.1016/j.prime.2022.100071.
49 49 C. Xu, K. Märker, J. Lee, A. Mahadevegowda, P. J. Reeves, S. J. Day, M. F. Groh, S. P. Emge, C. Ducati, B. Layla Mehdi, C. C. Tang and C. P. Grey, *Nat Mater*, 2021, **20**, 84–92.
50 50 J. Lamb, L. Stokes and A. Manthiram, *Chemistry of Materials*, 2020, **32**, 7389–7396.
51 51 S. Lou, Y. Zhao, J. Wang, G. Yin, C. Du and X. Sun, *Small*, 2019, 15.
52 52 B. Aktekin, R. Younesi, W. Zipprich, C. Tengstedt, D. Brandell and K. Edström, *J Electrochem Soc*, 2017, **164**, A942–A948.
53 53 R. Tian, P. J. King, J. Coelho, S. H. Park, D. V. Horvath, V. Nicolosi, C. O'Dwyer and J. N. Coleman, *J Power Sources*, DOI:10.1016/j.jpowsour.2020.228220.

Data Availability Statement

The datasets generated during and/or analyzed during the current study are available from the authors on reasonable request.